

Supporting Information

Selective Electrocatalytic Reduction of Carbon Dioxide to Methane by Guanidine-based Metal-Organic Cage

Ziang Zhang, Yang Yang, Jinfeng Wang, Xu Jing* and Chunying Duan

School of Chemistry, Dalian University of Technology, Dalian 116024, China.

Corresponding to: Xu Jing, xjing@dlut.edu.cn

Table of contents

1. Supplementary methods
2. Synthesis section
3. Single crystal X-ray crystallography
4. Characterization of Catalysis and mononuclear complexes
5. Interaction of host-guest
6. Electrocatalytic CO₂ reduction experiments
7. Detection of electrochemical CO₂RR products
8. NMR spectra
9. Computational simulation
10. References

1. Supplementary methods

Materials preparation.

All chemicals are of reagent grade quality and were obtained from commercial sources. All operations were performed under dry argon atmosphere using Schlenk and vacuum techniques. Solvents were dried using activated grade 3Å molecular sieves. Electrocatalytic systems such as electrochemical electrolytic cells (H-cells and flow cells) were purchased from Gaossunion.

Experimental parameter computational formulas.

Calculations of faradaic efficiencies of gaseous products¹: The gas products were collected by using the 1 mL injector without air, and then injected into gas chromatography. The Faradaic efficiency (FE) of gaseous product is:

$$FE = \frac{n N F}{Q} \times 100\%$$

Q: the charge obtained from the test during CO₂ reduction (C), F: faradaic constant (96485 C/mol), N: the number of electrons required to generate the product, n: the moles of products (mol). For the product of H₂, CO and CH₄, the N are 2, 2 and 8, respectively.

Calculations of TON, TOF and Selectivity of products²:

The turnover number was calculated by the equation:

$$TON = \frac{n_{pro.}}{n_{cat.}}$$

n_{pro.} represents the amounts of the product (mol), n_{cat.} represents the amounts of catalyst (mol).

The turnover efficiency was calculated by the equation:

$$TOF = \frac{TON}{t}$$

TON represents the turnover number, t represents the time of the reaction (h).

The selectivity was calculated by the equation:

$$Selectivity = \frac{n_1}{n_t} \times 100\%$$

n₁ represents the amounts of a target product (mol), n_t represents the amounts of total product (mol).

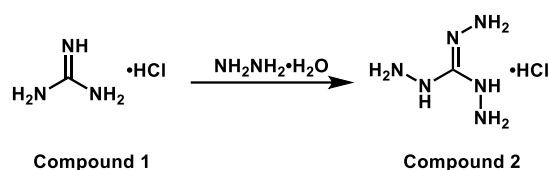
Stokes-Einstein equation³:

The Stokes-Einstein equation quantitatively describes the relationship between the self-diffusion coefficient D and its motion resistance in the fluid. When the self-diffusion coefficient of a given molecular species is known, the effective size or weight information can be obtained under controlled conditions through this equation, in which k_b is the Boltzmann constant ($1.380649 \times 10^{-23} \text{ J K}^{-1}$), T is the absolute temperature (298.15 K), d is the hydrodynamic diameter, the viscosity η of CH_3OD is 0.544 mPa s at 298.15 K.

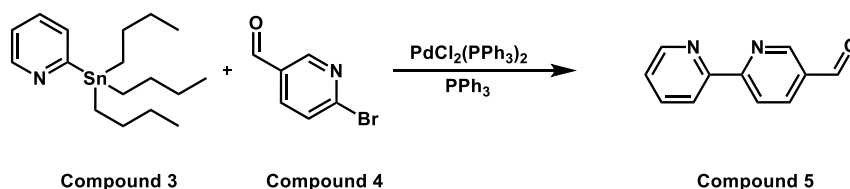
$$D = \frac{k_b T}{3\pi\eta d}$$

The self-diffusion coefficient of **H1** was $2.39 \times 10^{-10} \text{ m}^2 \cdot \text{s}^{-1}$ in CD_3OD solution.

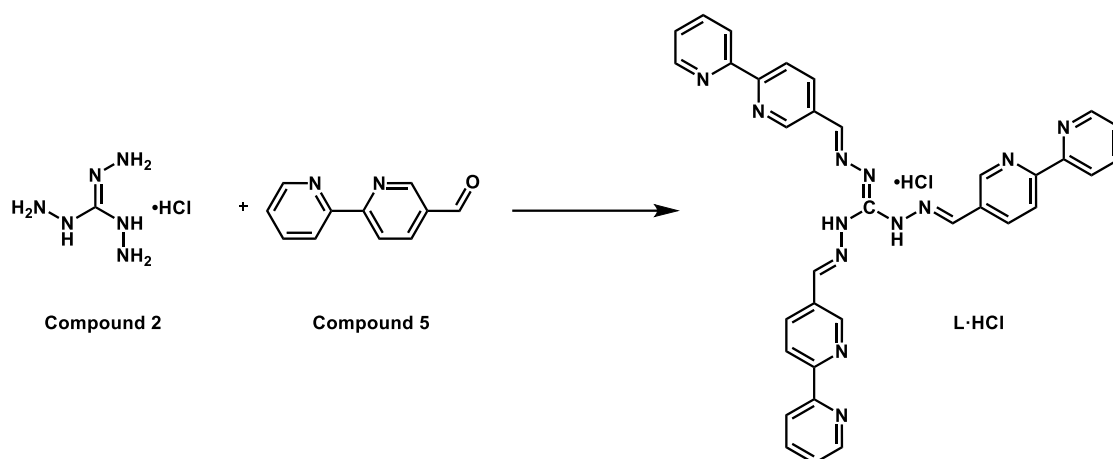
2. Synthesis section



Synthesis of Compound 2:⁴ Compound 1 (5.00 g, 52.3 mmol) was dissolved in 25 mL of 1,4-dioxane. Then, 8.5 mL of hydrazine hydrate was added, and the resulting solution was stirred under reflux for 2 hours. After cooling to room temperature, the white precipitate was filtered. The precipitate was then washed with 10 mL of 1,4-dioxane, dried, and compound 2 was obtained as a white powder. Yield: 95%. ¹H NMR (400 MHz, D₂O) δ 7.72 –7.66 (s, 6H), 6.92 (s, 3H).



Synthesis of Compound 5:⁵ Compound 3 (4.7 mL, 14.7 mmol), Compound 4 (3.3 g, 17.7 mmol), bis(triphenylphosphine) palladium(II) chloride (520 mg, 0.74 mmol), and triphenylphosphine (385mg, 1.47 mmol) were added together into 250 mL toluene solution. The reaction mixture was stirred under reflux for 72 hours under an argon atmosphere. After the reaction was completed, it was cooled to room temperature, and the solvent was removed by rotary evaporation, yielding a black oily liquid. The resulting solid was dissolved in 100 mL of dichloromethane and washed with 75 mL of saturated ammonium chloride solution. The aqueous phase was extracted with dichloromethane, and the organic phases were combined and evaporated to obtain the crude product. The crude product was purified by column chromatography (eluent: ethyl acetate/dichloromethane/cyclohexane in a ratio of 1/1/3), getting white powdered product. Yield: 55%. ¹H NMR (400 MHz, DMSO-*d*₆) δ 10.17 (s, 1H), 9.19 (dd, *J* = 2.1, 0.9 Hz, 1H), 8.76 (ddd, *J* = 4.8, 1.8, 0.9 Hz, 1H), 8.60 (d, *J* = 8.2 Hz, 1H), 8.49 (dt, *J* = 7.9, 1.1 Hz, 1H), 8.39 (dd, *J* = 8.2, 2.1 Hz, 1H), 8.02 (td, *J* = 7.7, 1.8 Hz, 1H), 7.55 (ddd, *J* = 7.5, 4.7, 1.2 Hz, 1H).



Synthesis of **L**: Compound **2** (70 mg, 0.5 mmol) and Compound **5** (0.276 g, 1.5 mmol) were dissolved in 3 mL of water and 20 mL of ethanol, respectively, and then mixed together. The mixture was stirred under reflux conditions for 6 hours. After completion of the reaction, it was filtered while hot. The precipitate was washed with hot anhydrous ethanol (10 mL) and dried to obtain the ligand without further purification. Yield: 40%. ^1H NMR (400 MHz, DMSO- d_6) δ 12.50 (s, 3H), 9.25 (d, $J = 1.2$ Hz, 3H), 8.88 (s, 3H), 8.76 (ddd, $J = 4.8, 1.8, 1.0$ Hz, 3H), 8.63 (dd, $J = 8.4, 2.1$ Hz, 3H), 8.57 (d, $J = 8.3$ Hz, 3H), 8.48 (d, $J = 7.9$ Hz, 3H), 8.02 (td, $J = 7.6, 1.8$ Hz, 3H), 7.58 – 7.50 (m, 3H). ^{13}C NMR (126 MHz, DMSO- d_6) δ 156.98, 154.72, 149.91, 149.74, 149.48, 148.97, 137.82, 136.13, 129.54, 125.05, 121.36, 120.63.

Synthesis of single crystal **H1**: Ligand **L** (25.5 mg, 0.04 mmol) and iron(II) trifluoromethanesulfonate (17.7 mg, 0.05 mmol) were dissolved in anhydrous methanol/anhydrous acetonitrile (20 mL/5 mL). The mixture was stirred under reflux for 24 hours under the protection of argon gas. After centrifugation, the supernatant was filtered through a filter. 2 mL of the solution was transferred into a 20 mL test tube, which was sealed with plastic film and raw tape. The test tube was placed in a wide-mouth bottle, and 150-200 mL of ether was added. The bottle was sealed, and the crystal was obtained by standing at room temperature for two weeks. Yield: 30%. HRMS (ESI) m/z calc. for $[\text{Fe}_4\text{L}_4(\text{OTf})_2]^{6+}$ 488.6008, found: 488.6008; $[\text{Fe}_4\text{L}_4\cdot 3(\text{OTf})]^{5+}$ 616.1115, found: 616.1113; $[\text{Fe}_4\text{L}_4\cdot 3(\text{OTf})\cdot(\text{HOTf})]^{5+}$ 646.1035, found: 646.1028; $[\text{Fe}_4\text{L}_4\cdot 4(\text{OTf})]^{4+}$ 807.3775, found: 807.3786; $[\text{Fe}_4\text{L}_4\cdot 4(\text{OTf})\cdot(\text{HOTf})]^{4+}$ 844.8675, found: 844.8645; $[\text{Fe}_4\text{L}_4\cdot 5(\text{OTf})]^{3+}$ 1126.1542, found: 1126.1520; $[\text{Fe}_4\text{L}_4\cdot 5(\text{OTf})\cdot(\text{HOTf})]^{3+}$ 1176.4727, found: 1176.4743.

Synthesis of the mononuclear iron complex **M1**: Dissolve 2,2'-bipyridine (23.4 mg, 0.15 mmol) and iron(II) trifluoromethanesulfonate (17.7 mg, 0.05 mmol) in 25 mL of anhydrous methanol and reflux for 24 hours under argon. Transfer 2 mL of the solution to a 20 mL test tube and seal with plastic wrap and PTFE tape. Place the tube in a wide-mouth flask, add 150 mL of ether and seal. After being left in the dark for two weeks, crystals were obtained. Yield: 90%. HRMS (ESI) m/z calc. for $[\text{Fe}(\text{bpy})_3]^{2+}$ 262.0700, found: 262.0707.

3. Single crystal X-ray crystallography

Table S1. Single Crystal X-ray Crystallography for **H1**.

Compound	Fe ₄ L ₄ (H1)
CCDC number	2402994
Formula	Fe ₄ (C ₃₄ N ₁₂ H ₂₆) ₄ (CF ₃ SO ₃) ₈
M _r (g/mol)	3824.3150
Crystal system	Trigonal
Space group	<i>R</i> 32
<i>a</i> (Å)	25.632(2)
<i>b</i> (Å)	25.632(2)
<i>c</i> (Å)	115.290(11)
<i>α</i> (°)	90
<i>β</i> (°)	90
<i>γ</i> (°)	120
Volume (Å ³)	65595(12)
<i>Z</i>	564
<i>D</i> _{calcd} (g/cm ³)	1.046
<i>μ</i> (Mo-K α , mm ⁻¹)	0.394
<i>F</i> (000)	21024
T (K)	120
R _{int}	0.0541
<i>wR</i> ₂ (all data)	0.2137
<i>R</i> _I [<i>I</i> > 2 σ (<i>I</i>)]	0.0666
Goodness of fit	1.036

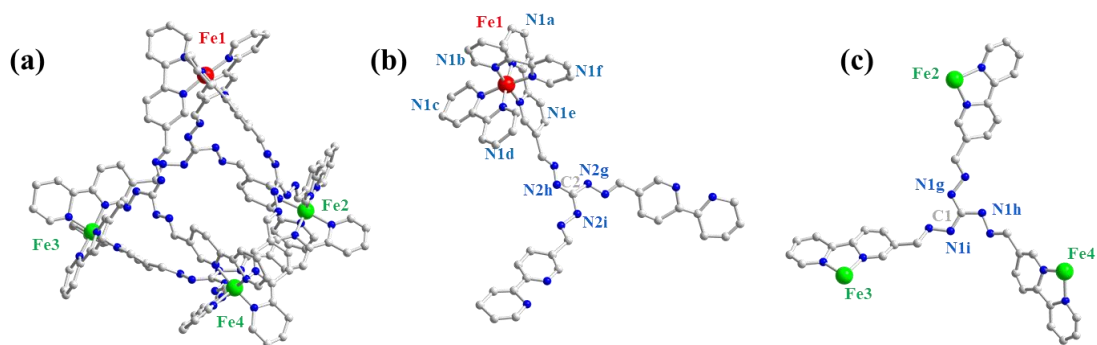


Figure S1. The crystal structure of **H1**. (Red balls and green balls: Fe; blue balls: N; grey balls: C) (a) Crystal structure diagram of **H1**. (b) A facet of **H1**. (c) The underside of **H1**.

Table S2. Selective bond distance (\AA) for **H1**.

Atom-Atom	Length (\AA)
Fe(1)–N(1a)	1.9547(36)
Fe(1)–N(1b)	1.9547(50)
Fe(1)–N(1c)	1.9547(53)
Fe(1)–N(1d)	1.9574(35)
Fe(1)–N(1e)	1.9574(48)
Fe(1)–N(1f)	1.9574(51)
C(2)–N(2g)	1.409(9)
C(2)–N(2h)	1.3334(121)
C(2)–N(2i)	1.3348(129)
Fe(1)–Fe(2)	14.5273(29)
Fe(1)–Fe(3)	14.5273(30)
Fe(1)–Fe(4)	14.5273(30)
Fe(2)–Fe(3)	14.4006(22)
Fe(3)–Fe(4)	14.4006(16)
Fe(2)–Fe(4)	14.4006(24)
C(1)–N(1g)	1.3141(75)
C(1)–N(1h)	1.3141(59)
C(1)–N(1i)	1.3141(93)

Table S3. Selective bond angle (°) for **H1**.

Atom-Atom-Atom	Bond angle (°)
N(1a)–Fe(1)–N(1b)	97.320(189)
N(1a)–Fe(1)–N(1c)	97.320(166)
N(1a)–Fe(1)–N(1d)	175.186(159)
N(1a)–Fe(1)–N(1e)	80.998(182)
N(1a)–Fe(1)–N(1f)	87.384(161)
N(1b)–Fe(1)–N(1c)	97.320(189)
N(1b)–Fe(1)–N(1d)	87.384(182)
N(1b)–Fe(1)–N(1e)	175.186(194)
N(1b)–Fe(1)–N(1f)	80.998(191)
Fe(1)–Fe(2)–Fe(3)	60.288(10)
Fe(2)–Fe(1)–Fe(3)	59.424(11)
Fe(2)–Fe(3)–Fe(4)	60.000(9)

Table S4. Single Crystal X-ray Crystallography for **M1**.

Compound	Fe(bpy) ₃ (M1)
CCDC number	2404614
Formula	Fe(C ₁₀ H ₈ N ₂) ₃ (CF ₃ SO ₃) ₂
M _r (g/mol)	822.0447
Crystal system	Monoclinic
Space group	<i>C2/c</i>
<i>a</i> (Å)	23.464(2)
<i>b</i> (Å)	13.6408(12)
<i>c</i> (Å)	23.002(2)
β (°)	103.909(3)
Volume (Å ³)	7146.3(11)
<i>Z</i>	8
<i>D</i> _{calcd} (g/cm ³)	1.589
μ (Mo-K α , mm ⁻¹)	0.627
<i>F</i> (000)	3488
T (K)	120
R _{int}	0.0794
<i>wR</i> ₂ (all data)	0.1088
<i>R</i> ₁ [<i>I</i> > 2 σ (<i>I</i>)]	0.0443
Goodness of fit	1.021



Figure S2. The crystal structure of **M1**. (Green ball: Fe; blue balls: N; grey balls: C)

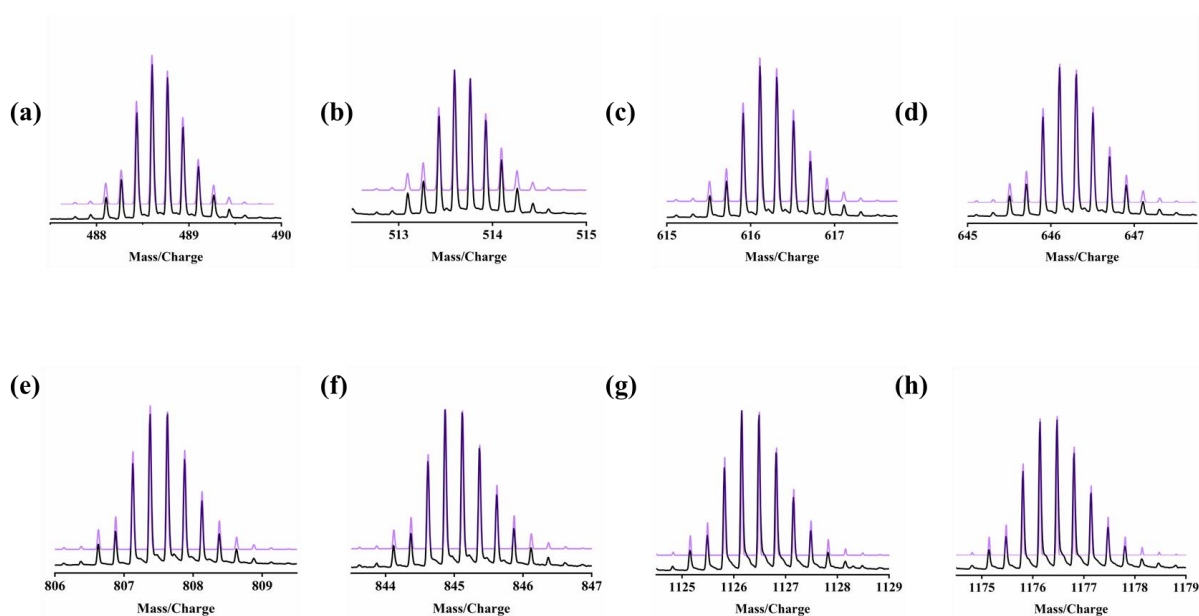
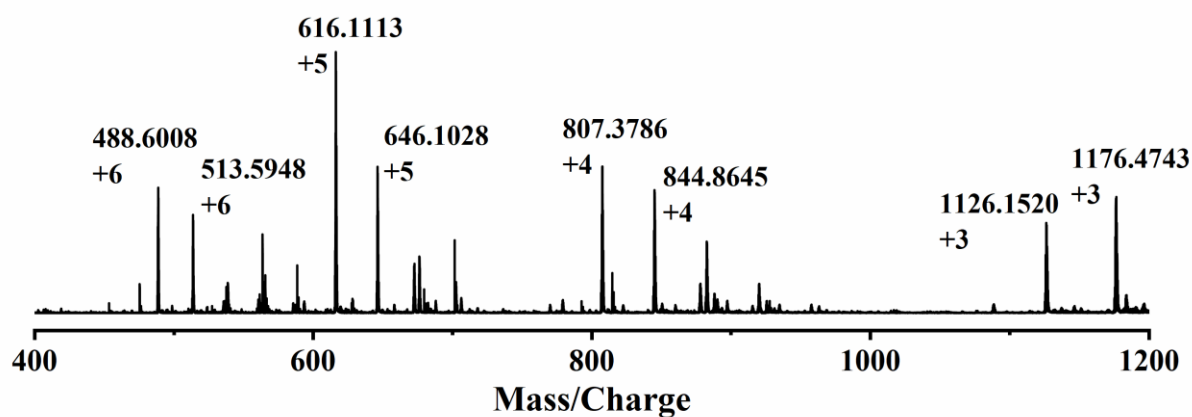
Table S5. Selective bond distance (Å) for **M1**.

Atom–Atom	Length (Å)
Fe–N(1)	1.9709(24)
Fe–N(2)	1.9632(19)
Fe–N(3)	1.9672(20)
Fe–N(4)	1.9664(23)
Fe–N(5)	1.9630(19)
Fe–N(6)	1.9697(19)

Table S6. Selective bond angle (°) for **M1**.

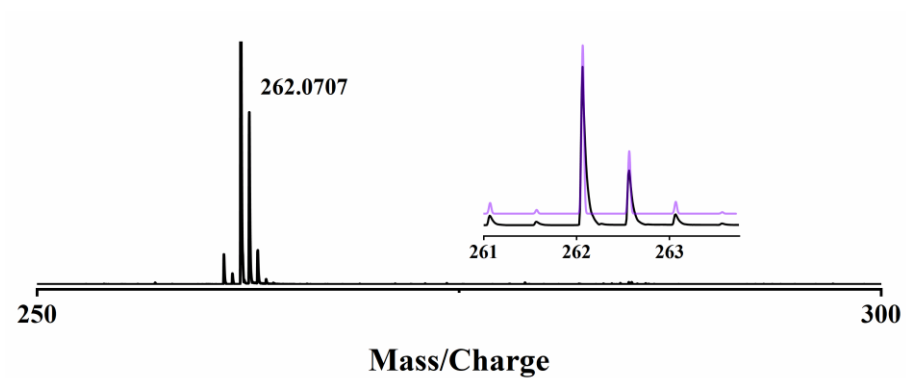
Atom–Atom–Atom	Angle (°)
N(1)–Fe–N(2)	95.046(85)
N(1)–Fe–N(3)	93.236(88)
N(1)–Fe–N(4)	175.026(90)
N(1)–Fe–N(5)	88.992(85)
N(1)–Fe–N(6)	81.839(87)

4. Characterization of Catalysis and mononuclear complexes



Peak	Value of m/z	Specie assigned
1	488.6008	$[(\text{Fe}_4\text{L}_4)\cdot 2\text{OTf}]^{6+}$
2	513.5948	$[(\text{Fe}_4\text{L}_4)\cdot 2\text{OTf}\cdot (\text{HOTf})]^{6+}$
3	616.1113	$[(\text{Fe}_4\text{L}_4)\cdot 3\text{OTf}]^{5+}$
4	646.1028	$[(\text{Fe}_4\text{L}_4)\cdot 3\text{OTf}\cdot (\text{HOTf})]^{5+}$
5	807.3786	$[(\text{Fe}_4\text{L}_4)\cdot 4\text{OTf}]^{4+}$
6	844.8645	$[(\text{Fe}_4\text{L}_4)\cdot 4\text{OTf}\cdot (\text{HOTf})]^{4+}$
7	1126.1520	$[(\text{Fe}_4\text{L}_4)\cdot 5\text{OTf}]^{3+}$
8	1176.4743	$[(\text{Fe}_4\text{L}_4)\cdot 5\text{OTf}\cdot (\text{HOTf})]^{3+}$

Figure S3. ESI-MS spectra of **H1** in methanol solution. The purple lines represent the results of the mass spectrum simulation. The table shows attribution of peaks.



Peak	Value of m/z	Specie assigned
1	262.0707	$[\text{Fe}(\text{bpy})_3]^{2+}$

Figure S4. ESI-MS spectra of **M1** in methanol solution. The purple line represents the result of the mass spectrum simulation.

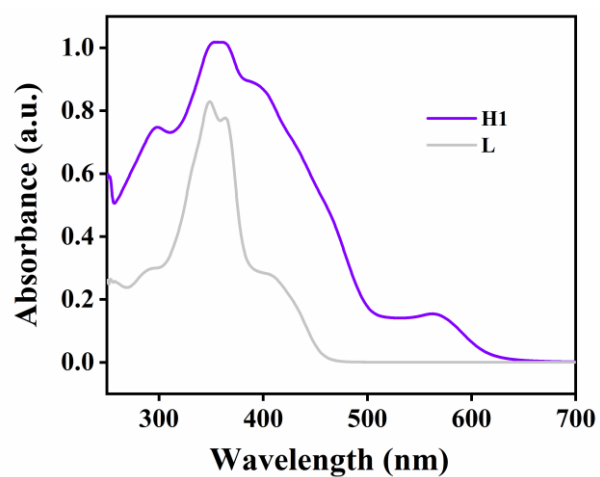


Figure S5. UV-vis absorption spectra in DMSO solution containing **H1** (0.006 mM), ligand **L** (0.05 mM), respectively.

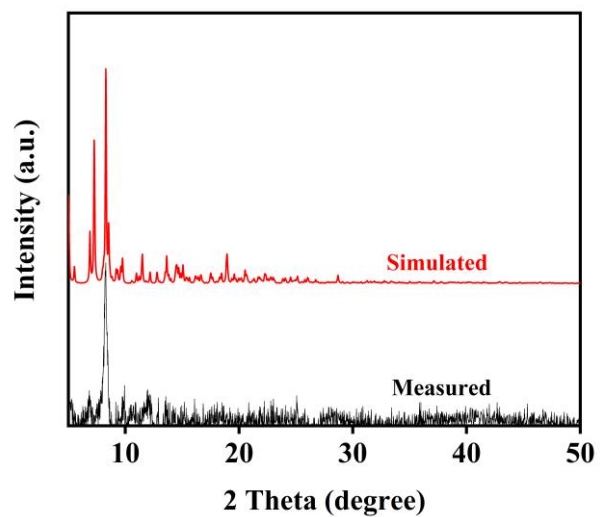


Figure S6. Experimental powder X-ray diffraction (PXRD) pattern of **H1**.

5. Interaction of host-guest.

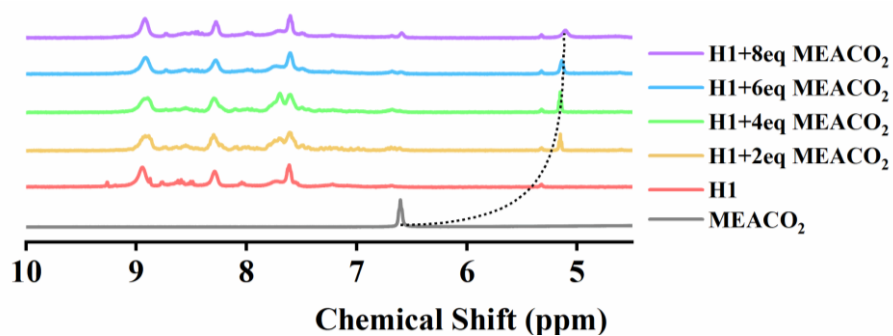


Figure S7. Nuclear magnetic titration experiments of **H1** and MEACO₂. ¹H NMR spectra in DMSO-d₆ solution containing 1 mM **H1** upon addition of MEACO₂. The ¹H NMR spectra (400 MHz, 298 K) showed that the addition of MEACO₂ to **H1** solution caused a high field shift of -OH from 6.60 ppm to 5.12 ppm.

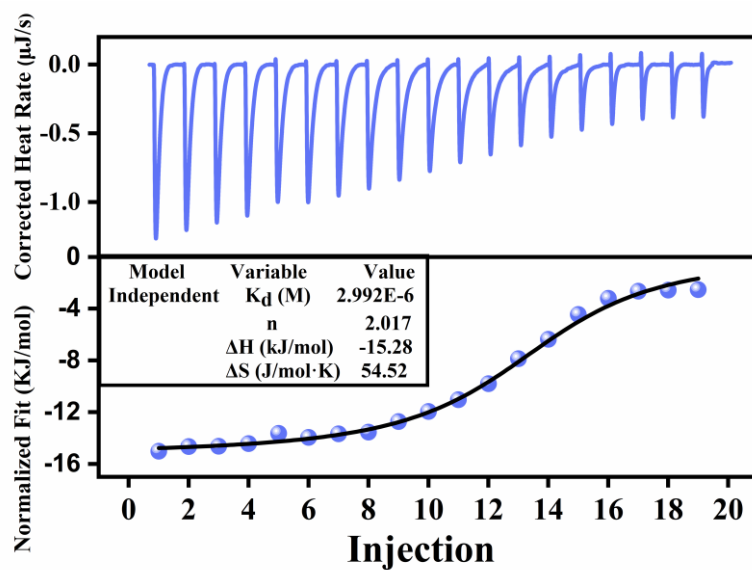


Figure S8. Microcalorimetric titration of the **H1** with MEACO₂ in DMSO solution at 298 K. Raw data for 20 sequential injections (10 μ L per injection) of MEACO₂ solution (1.0 mM) injected into the **H1** solution (0.1 mM). Apparent reaction heat obtained from the integration of calorimetric traces.

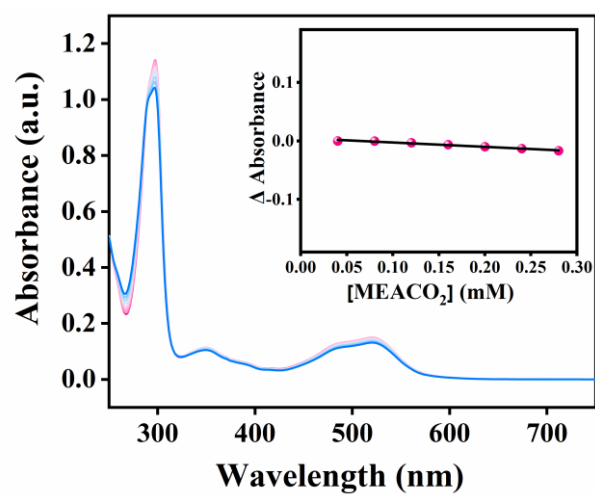


Figure S9. UV-vis titration experiments of **M1** and MEACO₂. (a) UV-vis absorption difference spectra in DMF solution containing **M1** (0.01 mM) upon addition of MEACO₂. (b) Plot of the absorbance changes at 520 nm. The solvent was dehydrated and the oxygen was removed by Ar.

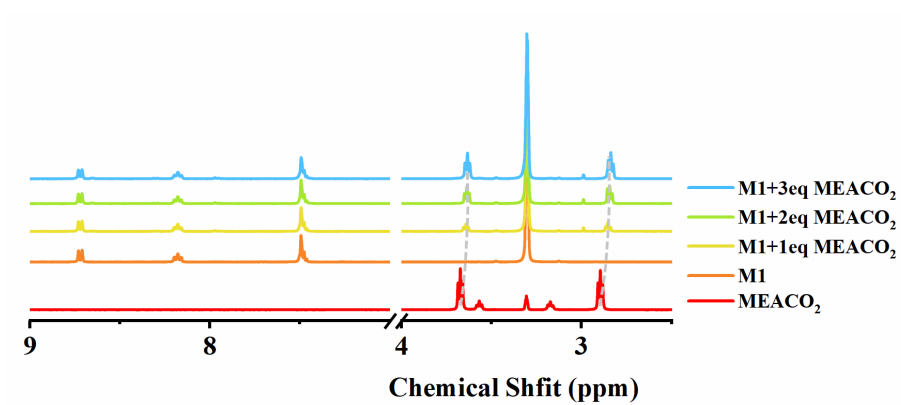


Figure S10. Nuclear magnetic titration experiments of **M1** and MEACO₂. ¹H NMR spectra in CD₃OD solution containing **M1** (0.01 mM) upon addition of MEACO₂. (400 MHz, 298 K)

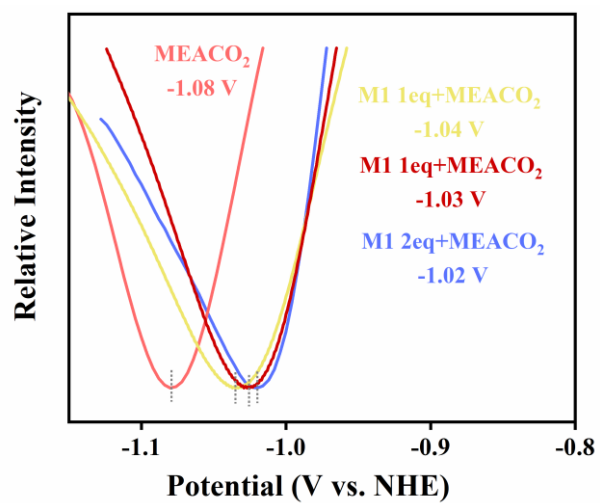


Figure S11. Electrochemical titration experiments of **M1** and MEACO₂. The SWV curves of **M1** in DMSO containing 0.1 M LiCl with MEACO₂ (0.1 mM). Scan rate: 0.05 V·s⁻¹.

6. Electrocatalytic CO₂ reduction experiments

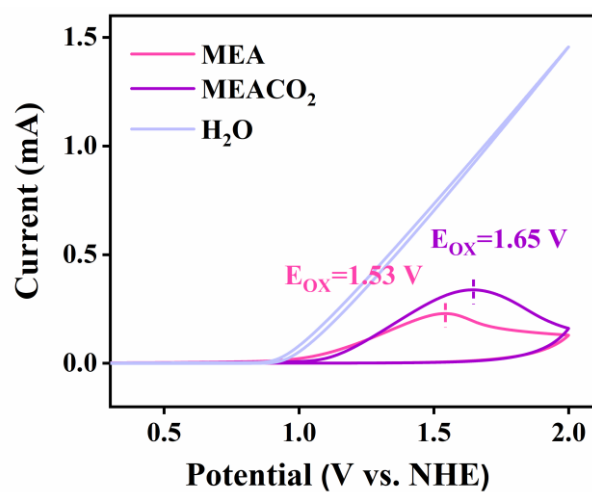


Figure S12. CV tests of anodic oxidation potential. CV curves of the H₂O, MEA and MEACO₂ in DMSO containing 0.1 M LiCl at 0.05 V·s⁻¹ scan rate. The oxidation potential of MEA is 1.53 V vs. NHE (MEACO₂: E_{OX} = 1.65 V vs. NHE), and the oxidation of H₂O appears faraday current from 0.90 V to 2.00 V vs. NHE.

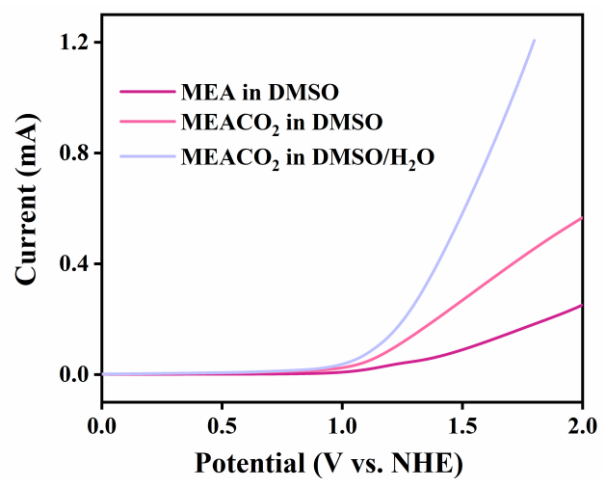


Figure S13. LSV tests of anodic oxidation potential. LSV curves of the MEA and MEACO₂ in DMSO and MEACO₂ in DMSO/H₂O (v:v = 2:1) containing 0.1 M LiCl at 0.05 V·s⁻¹ scan rate.



Figure S14. The oxygen evolution at the anode during the electrocatalytic experiment.

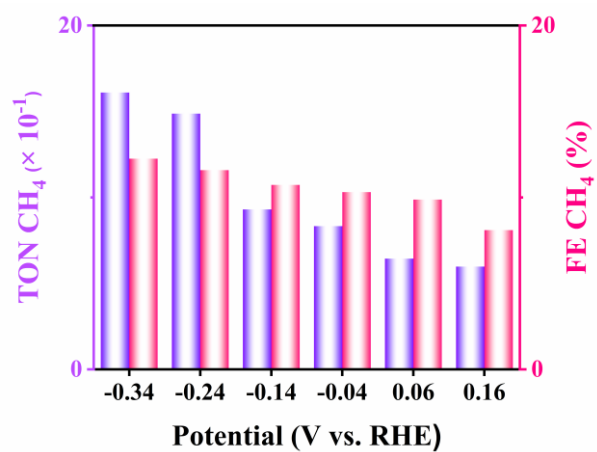


Figure S15. The FE and TON of methane produced by electrocatalytic CO₂RR under standard conditions for 2h without MEA in the H-type cell.

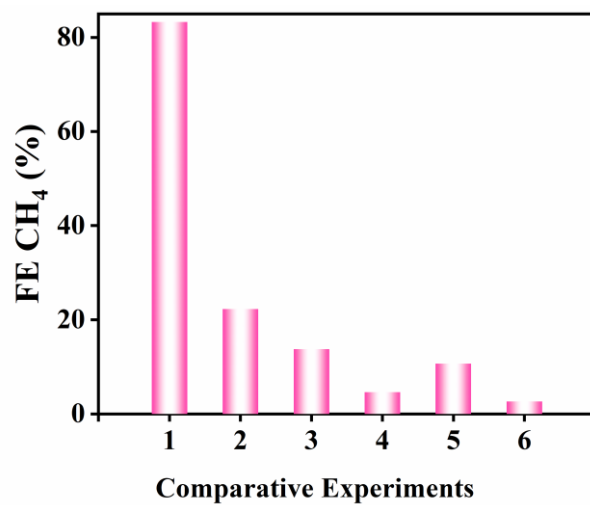


Figure S16. The FE of methane in comparison experiments at potential of -0.14 V vs. RHE.

Table S7. The FE and selectivity of methane in comparison experiments at potential of -0.14 V vs. RHE.

No.	Comparison experiments	FE CH ₄ %
1	Standard condition	83.30
2	M1 instead of H1	22.31
3	Fe(OTf) ₂ instead of H1	13.78
4	Ar instead of CO ₂	4.63
5	No MEA	15.72
6	No H1	2.67

Table S8. The FE of methane produced by **H1** electrocatalytic CO₂RR in comparison with other reported catalysts.

Number	Catalysts	Potential (V vs. RHE)	FE CH ₄ %	References
1	Fe₄L₄ (H1)	-0.04	69.8	this paper
2	GQD-NH ₂ -H	-0.84	70	ref. ⁶
3	Cu-Ce-O _x	-1.40	67.8	ref. ⁷
4	N-aGQDs	-0.98	63	ref. ⁸
5	Cu-SP-3F	-1.21	62	ref. ⁹
6	EDTA/CNT	-1.30	61.6	ref. ¹⁰
7	MAF-2P	-1.50	60	ref. ¹¹
8	Cu ₆₈ Ag ₃₂ nanowire	-1.17	60	ref. ¹²
9	7% Au-Cu	-1.06	58	ref. ¹³
10	La ₂ CuO ₄ perovskite	-1.40	56.3	ref. ¹⁴
11	CoO-2.5 nm/Cu/PTFE	-1.10	55	ref. ¹⁵
12	Cu-PzI	-1.00	52	ref. ¹⁶
13	Cu on PTFE	-1.42	50	ref. ¹⁷
14	Cu NCs	-1.50	48.3	ref. ¹⁸

7. Detection of electrochemical CO₂RR products.

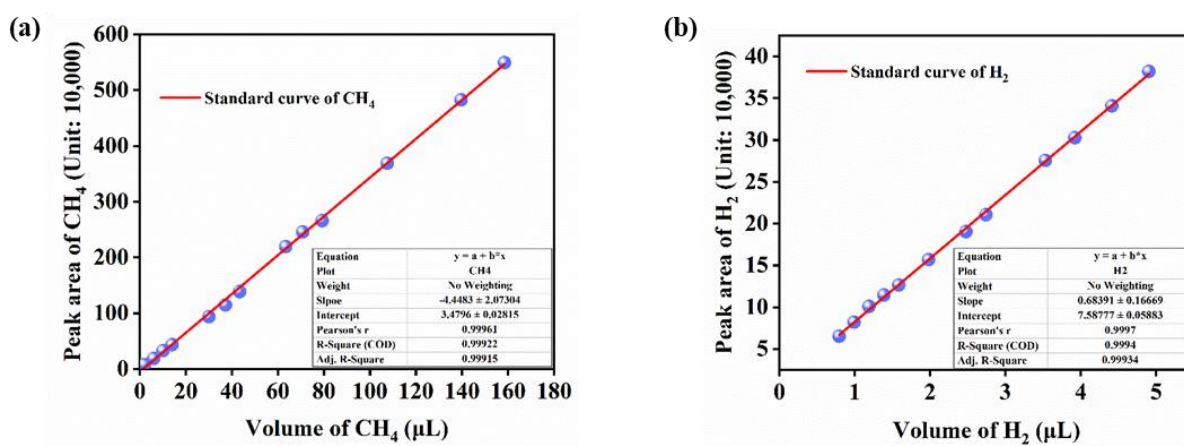


Figure S17. The fitting curves of CH₄ and H₂ were quantified by external standard method. (a) CH₄, (b) H₂.

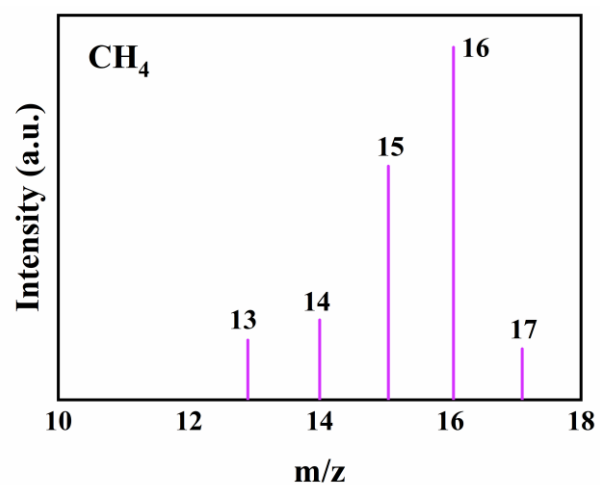


Figure S18. The GC-MS spectrum of CH₄ of **H1** electrolyzed for 2 h at -0.14 V vs. RHE in CO₂-saturated DMSO/H₂O (v/v = 2:1) containing 0.1 M LiCl, 2 M MEA and 0.01 mM **H1**. CH₄: m/z = 16.

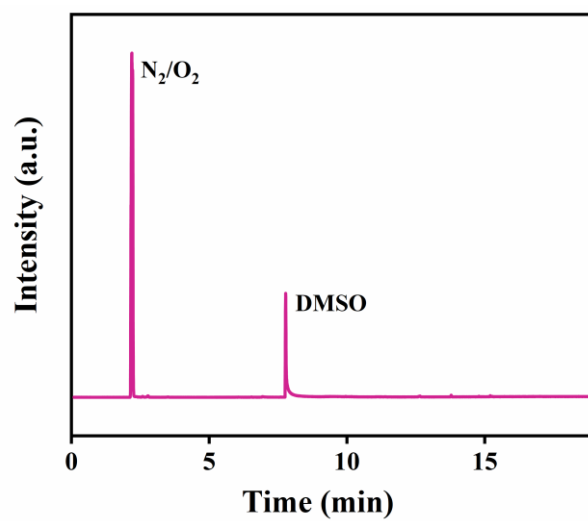


Figure S19. The HS-GC-MS spectrum of liquid products of **H1** electrolyzed for 2 h at -0.14 V vs. RHE in CO₂-saturated DMSO/H₂O (v/v = 2:1) containing 0.1 M LiCl, 2 M MEA and 0.01 mM **H1**. No liquid products of carbon dioxide reduction were detected.

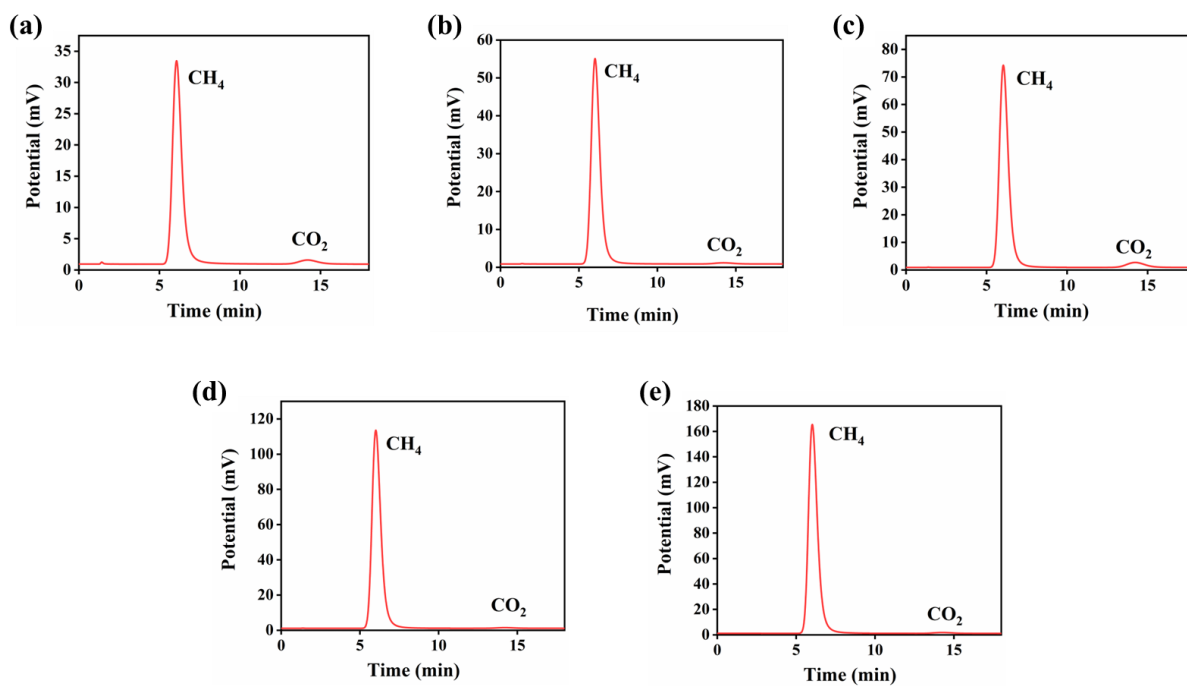


Figure S20. The GC spectra of gas products of **H1** electrolyzed for (a) 1.39 h, (b) 3.33h, (c) 4.56 h, (d) 7.89 h and (e) 18.33 h at -0.04 V vs. RHE in DMSO/H₂O (v/v = 2:1) containing 0.1 M LiCl, 2 M MEA and 0.01 mM **H1**.

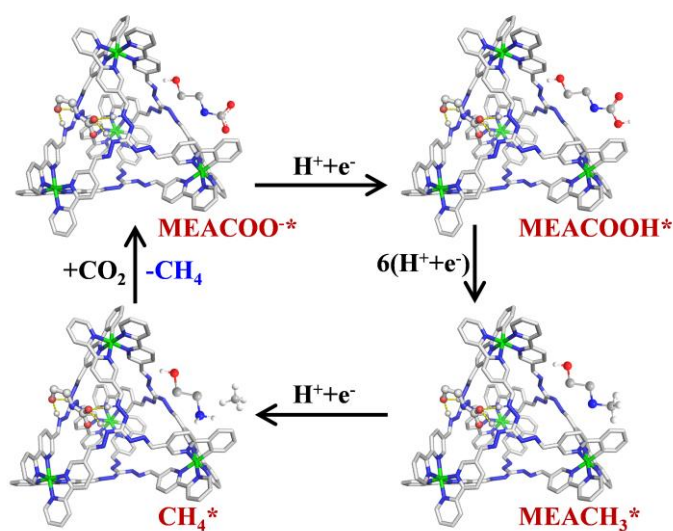
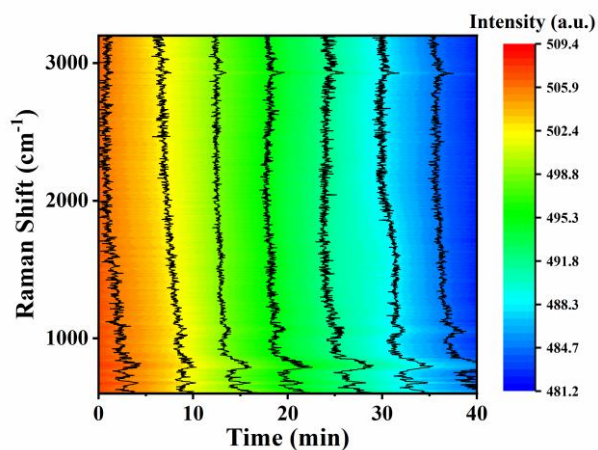


Figure S21. *In situ* Raman spectroscopy of CO₂RR process catalyzed by **H1** electrocatalysis under standard conditions and proposed mechanism. The peak at 800 cm⁻¹ was attributed to the SiO₂ in the quartz cell, which fluctuated significantly due to testing influences. All spectra were background-subtracted.

8. NMR spectra

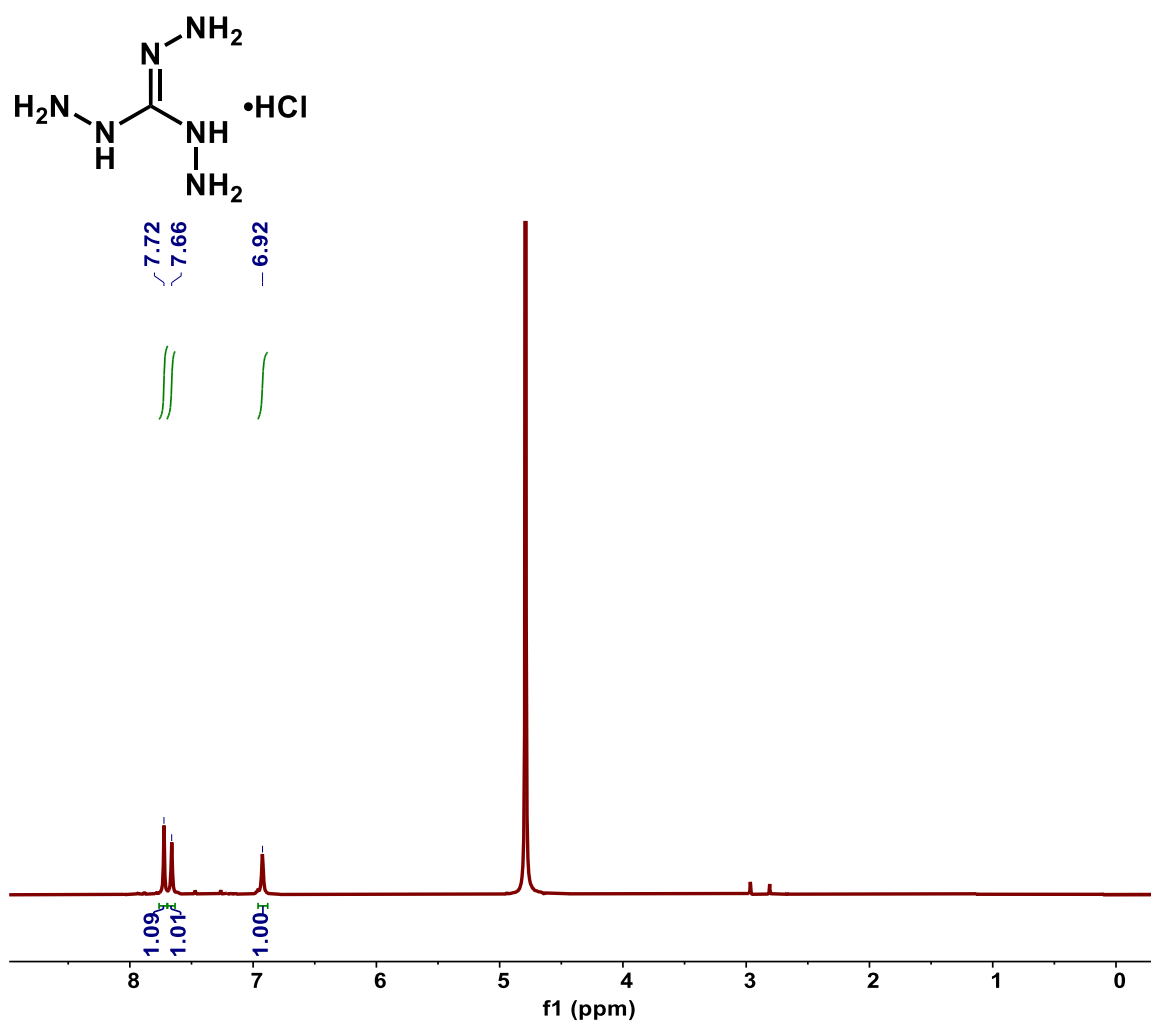


Figure S22. ^1H NMR spectra (400 MHz, 298 K, D_2O) of triaminoguanidine hydrochloride (Compound 2).

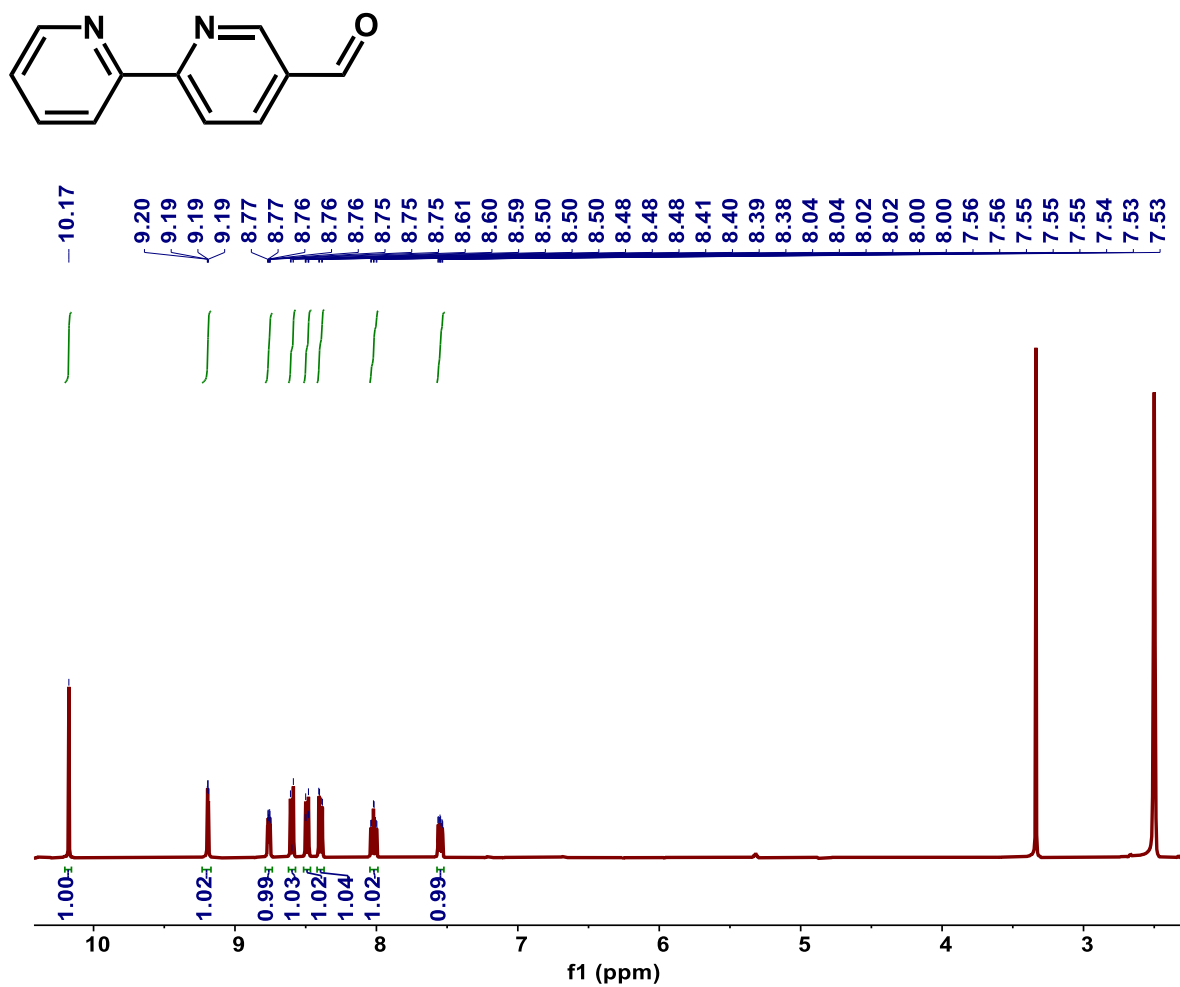


Figure S23. ¹H NMR spectra (400 MHz, 298 K, DMSO-d₆) of 2,2'-bipyridine-5-carbaldehyde (Compound 5).

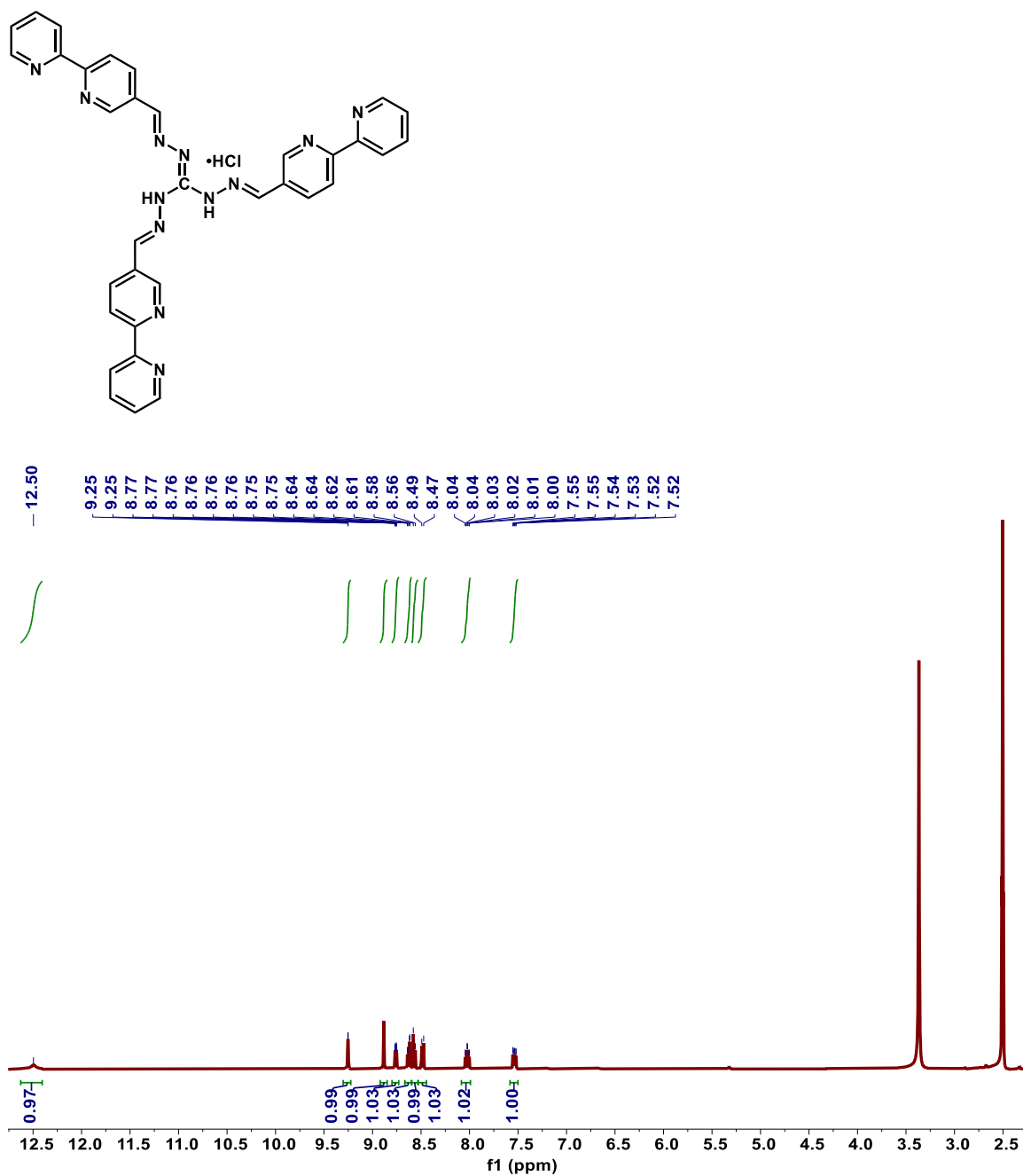


Figure S24. ¹H NMR spectra (400 MHz, 298 K, DMSO-d₆) of ligand L.

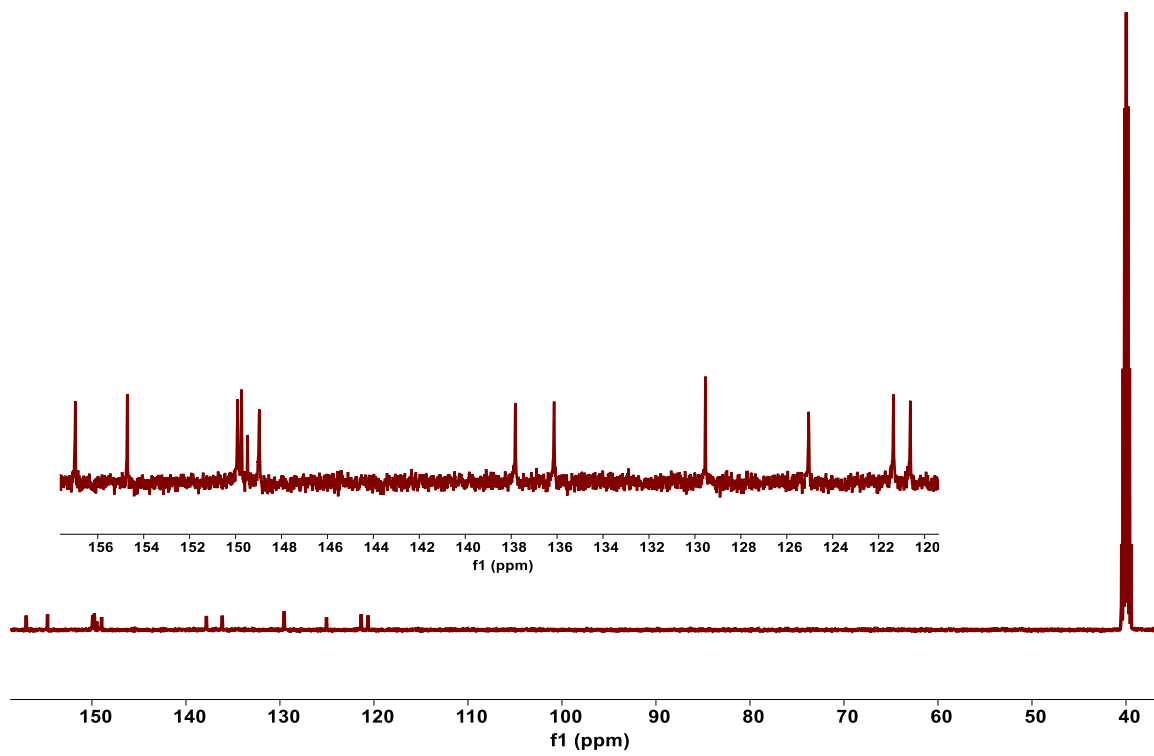


Figure S25. ^{13}C NMR spectra (126 MHz, 298 K, DMSO-d_6) of ligand L.

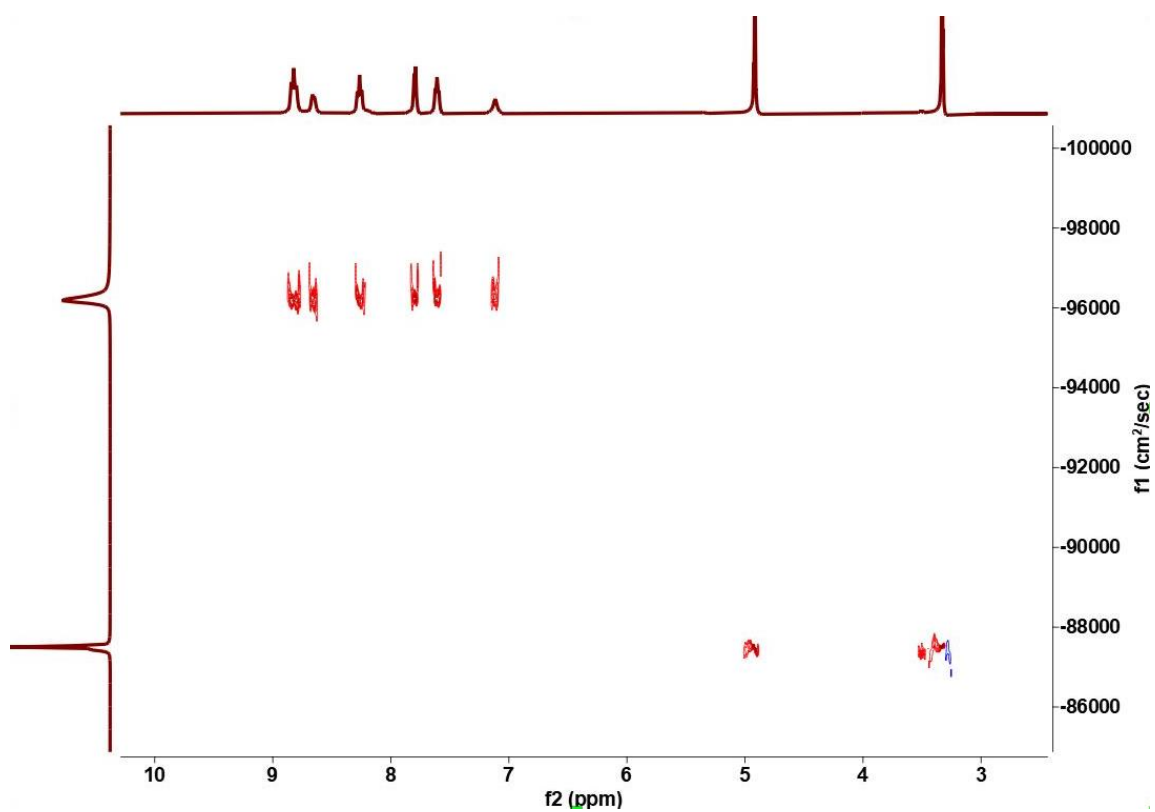


Figure S26. ¹H-DOSY (400 MHz, CD₃OD, 298 K) of **H1** (1.0 mM): $D = 2.39 \times 10^{-10} \text{ m}^2 \cdot \text{s}^{-1}$.

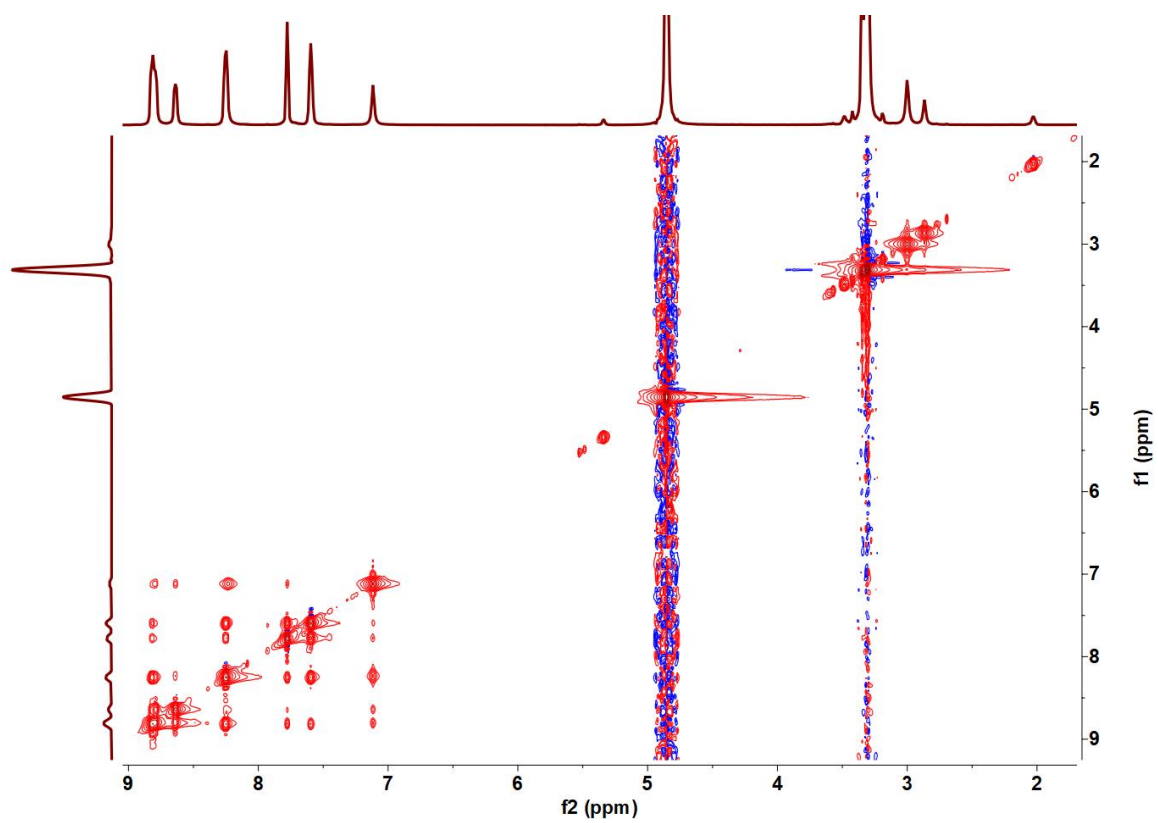


Figure S27. ^1H - ^1H NOESY (400 MHz, CD_3OD , 298 K) of **H1** (1.0 mM).

9. Computational simulation

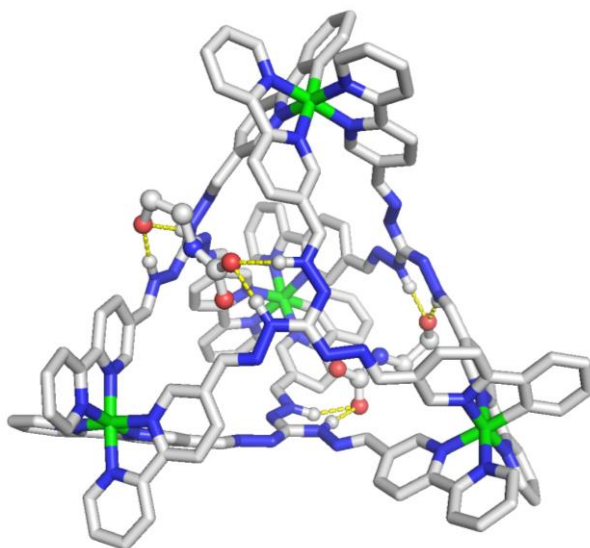


Figure S28. Computational simulation of host-guest interactions. The computational simulation of host-guest interactions was conducted using the AutoDock program 4.2. The structural data of the substrate was obtained from the PDB database. The molecular models were refined by removing hydrogen atoms and subsequently adding polar hydrogens. The processes of atom removal and addition were performed using AutoDock Tools. The configuration and orientation of the guest molecule, as well as the interaction sites between the guest and host molecules, were calculated using the Lamarckian genetic algorithm with default parameters. By comprehensively considering factors such as chemical rationality, aggregation state, and binding energy during host-guest complexation, the optimal host-guest inclusion model was ultimately obtained.

10. References

1. C. Chen, X. Yan, Y. Wu, S. Liu, X. Zhang, X. Sun, Q. Zhu, H. Wu and B. Han, Boosting the productivity of electrochemical CO₂ reduction to multi-carbon products by enhancing CO₂ diffusion through a porous organic cage, *Angew. Chem. Int. Ed.*, 2022, **61**, e202202607.
2. Z. Wen, S. Xu, Y. Zhu, G. Liu, H. Gao, L. Sun, F. Li, Aqueous CO₂ reduction on Si photocathodes functionalized by cobalt molecular catalysts/carbon nanotubes, *Angew. Chem. Int. Ed.*, 2022, **61**, e202201086.
3. Z. Wei, X. Jing, Y. Yang, J. Yuan, M. Liu, C. He, C. Duan, A platinum (II)-based molecular cage with aggregation-induced emission for enzymatic photocyclization of alkynylaniline, *Angew. Chem. Int. Ed.*, 2023, **62**, e202214577.
4. P. Howlader, S. Mondal, S. Ahmed and P. S. Mukherjee, Guest-induced enantioselective self-assembly of a Pd₆ homochiral octahedral cage with a C₃-symmetric pyridyl donor, *J. Am. Chem. Soc.*, 2020, **142**, 50, 20968-20972.
5. Y. Yang, H. Li, X. Jing, Y. Wu, Y. Shi and C. Duan, Dye-loaded metal-organic helical capsules applied to the combination of photocatalytic H₂S splitting and nitroaromatic hydrogenation, *Chem. Commun.*, 2022, **58**, 807-810.
6. T. Zhang, W. Li, K. Huang, H. Guo, Z. Li, Y. Fang, R. M. Yadav, V. Shanov, P. M. Ajayan, L. Wang, C. Lian and J. Wu, Regulation of functional groups on graphene quantum dots directs selective CO₂ to CH₄ conversion, *Nat. Commun.*, 2021, **12**, 5265.
7. X. Zhou, J. Shan, L. Chen, B. Xia, T. Ling, J. Duan, Y. Jiao, Y. Zheng and S. Qiao, Stabilizing Cu²⁺ ions by solid solutions to promote CO₂ electroreduction to methane, *J. Am. Chem. Soc.*, 2022, **144**, 2079-2084.
8. R. M. Yadav, Z. Li, T. Zhang, O. Sahin, S. Roy, G. Gao, H. Guo, R. Vajtai, L. Wang, P. M. Ajayan and J. Wu, Amine-functionalized carbon nanodot electrocatalysts converting carbon dioxide to methane, *Adv. Mater.*, 2022, **34**, 2105690.
9. S. Chen, B. Wang, J. Zhu, L. Wang, H. Ou, Z. Zhang, X. Liang, L. Zheng, L. Zhou, Y. Su, D. Wang, and Y. Li, Lewis acid site-promoted single-atomic Cu catalyzes electrochemical CO₂ methanation, *Nano Lett.*, 2021, **21**, 7325-7331.
10. M. Huang, S. Gong, C. Wang, Y. Yang, P. Jiang, P. Wang, L. Hu and Q. Chen, Lewis-basic EDTA as a highly active molecular electrocatalyst for CO₂ reduction to CH₄, *Angew. Chem. Int. Ed.*, 2021, **60**, 23002-23009.
11. L. Zhuo, P. Chen, K. Zheng, X. Zhang, J. Wu, D. Lin, S. Liu, Z. Wang, J. Liu, D. Zhou and J. Zhang, Flexible cuprous triazolate frameworks as highly stable and efficient electrocatalysts for CO₂ reduction with tunable C₂H₄/CH₄ selectivity, *Angew. Chem. Int. Ed.*, 2022, **61**, e202204967.
12. C. Chang, S. Lin, H. Chen, J. Wang, K. J. Zheng, Y. Zhu and H. M. Chen, Dynamic reoxidation/reduction-driven atomic interdiffusion for highly selective CO₂ reduction toward methane, *J. Am. Chem. Soc.*, 2020, **142**, 12119-12132.
13. X. Wang, P. Ou, J. Wicks, Y. Xie, Y. Wang, J. Li, J. Tam, D. Ren, J. Y. Howe, Z. Wang, A. Ozden, Y. Z. Finfrock, Y. Xu, Y. Li, A. S. Rasouli, K. Bertens, A. H. Ip, M. Graetzel, D. Sinton and E. H. Sargent, Gold-in-copper at low *CO coverage enables efficient electromethanation of CO₂, *Nat. Commun.*, 2021, **12**, 3387.
14. S. Chen, Y. Su, P. Deng, R. Qi, J. Zhu, J. Chen, Z. Wang, L. Zhou, X. Guo and B. Y. Xia, Highly selective carbon dioxide electroreduction on structure-evolved copper perovskite oxide toward methane production, *ACS Catal.*, 2020, **10**, 4640-4646.
15. Y. Li, A. Xu, Y. Lum, X. Wang, S. Hung, B. Chen, Z. Wang, Y. Xu, F. Li, J. Abed, J. E. Huang, A. S. Rasouli, J. Wicks, L. K. Sagar, T. Peng, A. H. Ip, D. Sinton, H. Jiang, C. Li and E. H. Sargent, Promoting CO₂ methanation via ligand-stabilized metal oxide clusters as hydrogendonating motifs, *Nat. Commun.*, 2020, **11**,

6190.

16. R. Wang, J. Liu, Q. Huang, L. Dong, S. Li, and Y. Lan, Partial coordination-perturbed Bi-Copper sites for selective electroreduction of CO₂ to hydrocarbons, *Angew. Chem. Int. Ed.*, 2021, **60**, 19829-19835.
17. X. Wang, A. Xu, F. Li, S. Hung, D. Nam, C. M. Gabardo, Z. Wang, Y. Xu, A. Ozden, A. S. Rasouli, A. H. Ip, D. Sinton and E. H. Sargent, Efficient methane electrosynthesis enabled by tuning local CO₂ availability, *J. Am. Chem. Soc.*, 2020, **142**, 3525-3531.
18. H. S. Jeon, J. Timoshenko, C. Rettenmaier, A. Herzog, A. Yoon, S. W. Chee, S. Oener, U. Hejral, F. T. Haase and B. R. Cuenya, Selectivity control of Cu nanocrystals in a gas-fed flow cell through CO₂ pulsed electroreduction, *J. Am. Chem. Soc.*, 2021, **143**, 7578-7587.